Calming the waves, not the storm: measuring the Kelvin–Helmholtz instability in a tangential magnetic field

Armin Kögel[1,†], Alexandra Völkel[1] and Reinhard Richter[1,†]

[1]Experimentalphysik 5, Universität Bayreuth, 95440 Bayreuth, Germany

We measure the Kelvin–Helmholtz instability in between a layer of a diamagnetic fluid flowing in a channel and a layer of ferrofluid resting on top. When the diamagnetic fluid exceeds a critical flow velocity the interface in between both fluids becomes unstable and waves develop. It has been predicted by Sutyrin & Taktarov (*J. Appl. Math. Mech.*, vol. 39, 1975, pp. 520–524) that a homogeneous magnetic field, oriented horizontally, stabilizes the liquid interface. To test this prediction we apply in a closed flow channel a local periodic perturbation of the interface by magnetic or mechanic means. From the measured growth and decay rates of the interface undulations we determine the critical flow velocity for various driving frequencies and applied magnetic fields. In this way we confirm quantitatively the stabilizing effect of the horizontal field. Moreover we measure the dispersion relation of the interfacial waves.

Key words: instability control, air/sea interactions, magnetic fluids

---

1. Introduction

And the same day, when the even was come, he saith unto them, Let us pass over unto the other side. 4:36 And when they had sent away the multitude, they took him even as he was in the ship. And there were also with him other little ships. 4:37 And there arose a great storm of wind, and the waves beat into the ship, so that it was now full. 4:38 And he was in the hinder part of the ship, asleep on a pillow: and they awake him, and say unto him, Master, carest thou not that we perish? 4:39 And he arose, and rebuked the wind, and said unto the sea, Peace, be still. And the wind ceased, and there was a great calm (Mark 4:35–39, KJV Emerald Text Bible 2006).

Indeed, since the beginning of navigation, men have been threatened by waves, generated by wind blowing over the surface of water. The velocity difference across the interface between the air and the water drives the waves, as was demonstrated in early experiments by von Helmholtz (1868) and his friend Lord Kelvin (Thomson 1871).

† Email addresses for correspondence: armin.koegel@uni-bayreuth.de, reinhard.richter@uni-bayreuth.de

Their seminal works have given rise to the term Kelvin–Helmholtz instability (KHI) for this phenomenon.

Besides being a hazard, water waves are also an economic nuisance. According to Scheidt (2012), sea disturbances increase the fuel consumption of ships on all oceans by 3 %. Apart from divine intervention, oil poured onto the sea calms the waves, as reported already by Aristotle, Plutarch and Pliny the Elder (Scott 1978). Landerer (1894) even conducted test experiments to discover which type of oil has the best effect. However, this method has become obsolete because of pollution control. In contrast, the calming effect of rain on sea disturbances (Tsimplis 1991) is harmless, but does not happen on schedule. However, externally applied electric and magnetic fields can be switched on at will. But due to the tiny magnetic susceptibility of diamagnetic water ($\chi \approx -10^{-5}$) the latter have no effect for sea disturbances.

The same is not true for ferrofluid, a colloidal dispersion of magnetic nanoparticles (Rosensweig 1985), which has a huge susceptibility in the range of $0 < \chi < 10$. It has been established both theoretically (Gailitis 1977; Friedrichs & Engel 2001) and experimentally (Cowley & Rosensweig 1967; Gollwitzer *et al.* 2007; Richter & Lange 2009) that a magnetic field oriented normally to the static liquid layer destabilizes the interface. In contrast, early experiments for the tilted field instability in a resting layer of ferrofluid (Barkov & Bashtovoi 1977; Bercegol *et al.* 1987) have shown that a horizontal field component can stabilize the interface. This has been quantitatively confirmed by theory (Friedrichs 2002) and experiments (Reimann *et al.* 2005; Groh *et al.* 2007).

Also for the KHI, the stabilizing effect of a tangential magnetic field, or more precisely the shift of the onset of the linear instability to higher flow velocities, was predicted in a seminal theoretical work by Sutyrin & Taktarov (1975). Later it was modelled by Rosensweig (1985), Malik & Singh (1992), Elhefnawy (1995) and Zakaria (2003). Whereas most models consider two layers of inviscid liquids in two dimensions, and are taking advantage of a velocity potential, more realistic calculations, such as those by Elhefnawy & Moatimid (2001), are few and far between. Taking into account viscosity, a three-dimensional confinement and a nonlinear magnetization curve, Yecko (2009, 2010) simulated a low Reynolds number channel flow and concluded that the 'stabilizing effect' of a tangential magnetic field may be an oversimplification. This calls for an experiment.

For fluid under motion, the stabilizing effect of a horizontal magnetic field has so far been measured only by Zelazo & Melcher (1969) for ferrofluid sloshing in a tank. To the best of our knowledge, the magnetic stabilization of the KHI for a magnetic liquid interface has never been explored experimentally in a macroscopic channel. This deficiency is somewhat surprising, because in plasma physics the stabilizing effect of magnetic fields on the KHI was examined in both theory (D'Angelo 1965) and experiment (D'Angelo & Goeler 1966) long ago. Especially in the plasma of the solar corona, magnetic stabilization has been observed to play an important role (Foullon *et al.* 2011). Recently Li *et al.* (2018) showed evidence of the KHI emerging in between solar blowout jets guided by magnetic flux tubes. This is happening in such a way that the magnetic field is inherently tangential to the interface between the flux tubes.

In this article we report on earthbound experiments for a magnetic liquid interface in order to fill the above-mentioned gap. The article is organized as follows. As an introduction for the reader we present in § 2 the governing equations. Next, in § 3, the experimental set-up and the ferrofluid are characterized. Besides exploring spontaneously emerging interface waves we want to investigate as well waves of well defined frequency (and wavenumber). Therefore we sketch in the same section two different methods of periodic wave excitation. Our experimental results are reported in § 4. From the measured
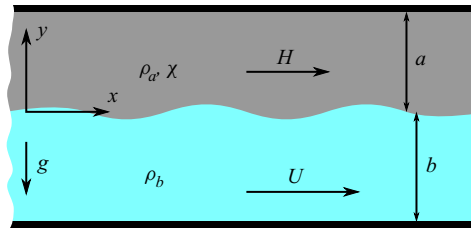
FIGURE 1. Illustrative sketch of the flow configuration.

growth and decay rates of the interface undulations we determine the critical flow velocity for various excitation frequencies and applied magnetic fields. In addition we use the driving to measure the dispersion relation of the interface waves. The article finishes with a summary, discussion, and outlook (§ 5).

2. Governing equations

To deduce the dispersion relation for interfacial waves one may assume a two-dimensional system as shown in figure 1. It consists of two superposed layers of inviscid immiscible fluids of different densities $\rho_a < \rho_b$. In agreement with the experiments the magnetic fluid with magnetic susceptibility χ is at rest in the top layer, whereas the diamagnetic fluid below is moving with constant velocity U. Note that this upside-down version of the classical arrangement ('wind blowing over the sea') is motivated by the availability of immiscible diamagnetic and superparamagnetic fluids (cf. § 3). For a flat interface the heights of the upper and lower layer are described by a and b, respectively. The interfacial tension γ between the two fluids is stabilizing the interface. Because we neglect viscosity and consequently shear stresses, we can assume a non-continuous velocity profile. We apply a homogeneous magnetic field of magnitude H parallel to the unperturbed interface. In a linear stability analysis all small disturbances from the basic state are analysed into normal modes, i.e. they are described by the function $A(x, t)$ in the coordinate system given in figure 1. A linear wave, propagating in direction of the flow, is described by

$$A(x, t) = A_0 \operatorname{Re}\{e^{i(kx-\omega t)}\}, \tag{2.1}$$

where the wavenumber k or the frequency ω can be complex, and one obtains a linear instability in space or time, respectively. An additional phase is not necessary for our purposes and can be omitted. For $\operatorname{Im}(\omega) > 0$, surface undulations will grow exponentially and the flat interface is unstable. Following the standard procedure of linear stability analysis, the dispersion relation of linear interface waves for semi-infinite layers can be derived (Sutyrin & Taktarov 1975; Rosensweig 1985), which reads in our notation

$$\omega^2 \rho_a + (\omega - kU)^2 \rho_b = kg(\rho_b - \rho_a) + k^3\gamma + k^2\tilde{\mu}H^2. \tag{2.2}$$

Here g denotes the gravitational acceleration, and $\tilde{\mu} = \mu_0\chi^2/(\chi + 2)$ is proportional to the vacuum permeability μ_0 and depends on the susceptibility χ. Note that we can neglect here the effect of the finite layer thicknesses a and b, because the observed wavenumbers are sufficiently high. The dispersion relation (2.2) can be written in the form

$$\omega_{1,2} = \underbrace{kU\frac{\rho_b}{\rho_a + \rho_b}}_{\hat{\omega}} \pm \underbrace{\sqrt{\frac{k^3\gamma}{\rho_a + \rho_b} - \frac{k^2U^2\rho_a\rho_b}{(\rho_a + \rho_b)^2} + \frac{k^2\tilde{\mu}H^2}{\rho_a + \rho_b} + kg\frac{\rho_b - \rho_a}{\rho_a + \rho_b}}}_{\tilde{\omega}}, \tag{2.3}$$
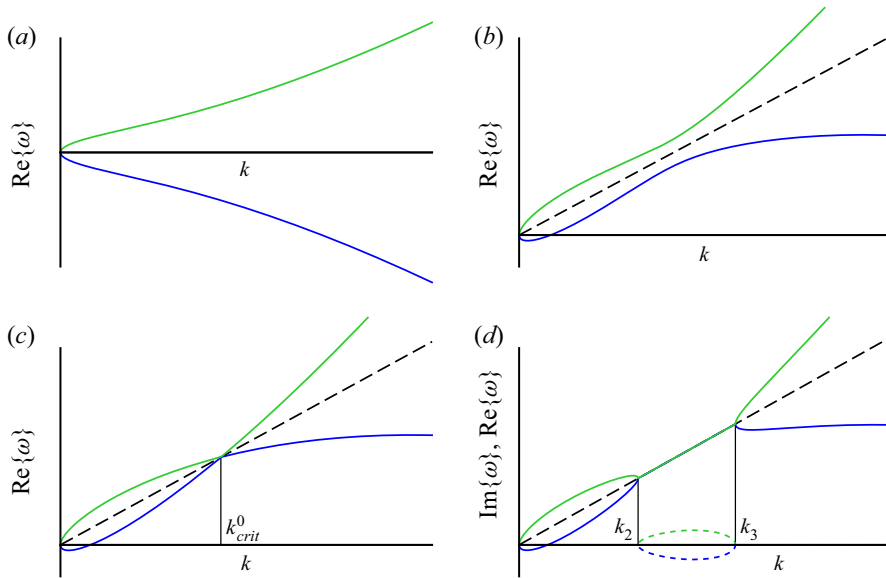
FIGURE 2. Dispersion relation $\omega(k)$ of interfacial waves illustrated for $H = 0$ kA m^{-1} and four different flow velocities U: $U = 0$ (a), $U \lesssim U_{crit}^0$ (b), $U = U_{crit}^0$ (c) and $U \gtrsim U_{crit}^0$ (d). The different colours show the two branches for ω_1 and ω_2. Solid lines represent the real part, dotted lines the imaginary part of ω. The dashed line represents the convective term $\hat{\omega}$.

giving a convenient equation for the instability in time. The right-hand side of (2.3) is made up of two terms. The first one, $\hat{\omega}$, describes a convective movement with the constant velocity ω/k proportional to the flow velocity U. It vanishes for $U = 0$ (see figure 2a), whereas it increases linearly with k for $U > 0$, as marked in figure 2(b–d) by a dashed black line. The second term, $\tilde{\omega}$, has a positive (negative) root, which is plotted in figure 2 by a green (blue) solid line, respectively. Under the root are three positive addends and one negative one. Both the second and the third addend depend on k^2. Obviously an increase in terms U^2 can be compensated by an increment in terms H^2. As long as $\tilde{\omega}$ is real, the amplitude of the wave remains the same. For a negative discriminant, however, $\tilde{\omega}$ becomes imaginary, which leads to a stable and an unstable branch in the dispersion relation. This destabilization occurs for a certain range of wavenumbers if the flow velocity U is sufficiently high. On the other hand we can stabilize the system by increasing the surface tension, the density difference or, in our case, the applied magnetic field.

Figure 2 shows the transition from a stable to a linearly unstable interface without an applied magnetic field. If $U = 0$ m s^{-1}, as displayed in figure 2(a), the dispersion relation is the same as for ordinary interface waves with a capillary and a gravitational term. The green (blue) branch is associated with waves moving in the positive (negative) direction, respectively. When we increase the flow velocity U the two branches move closer together (cf. panel b) and for the critical velocity U_{crit}^0 the branches touch each other at the critical wavenumber k_{crit}^0, as shown in panel (c). For higher velocities $U > U_{crit}^0$ there is a band of unstable wavenumbers between k_2 and k_3 (panel d).

Of special interest is not only the velocity of the first occurrence of unstable waves U_{crit}^0, but also the critical velocity U_{crit} for an arbitrary wavenumber k or wave frequency $f = \omega/2\pi$, corresponding to the *neutral curve*. The critical velocity depending on the wavenumber can be calculated by solving the equation $\tilde{\omega} = 0$ s^{-1} for the velocity U. It is
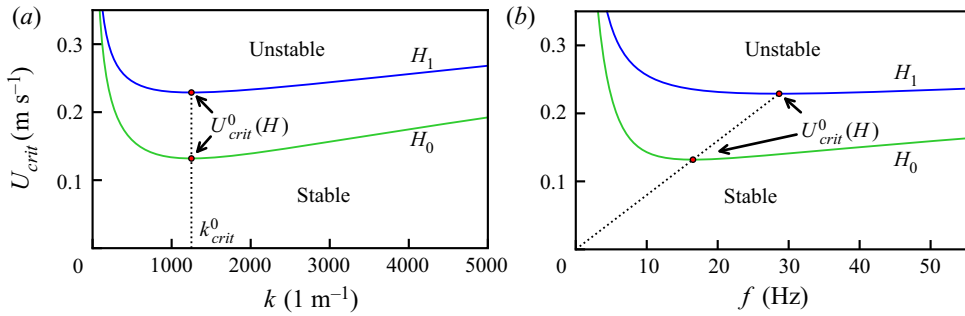
FIGURE 3. Stability maps for different magnetic fields $H_0 = 0$ kA m^{-1} (green line) and $H_1 = 10$ kA m^{-1} (blue line). For system parameters please see §3. The solid lines show the dependency of the critical velocity U_{crit} on the wavenumber k (a) and the frequency f (b). The dots mark the wavenumbers and frequencies of the first occurrence of the instability. The dotted lines connect these points.

given by

$$U_{crit}(k, H) = \sqrt{\frac{\rho_a + \rho_b}{\rho_a \rho_b} \left(k\gamma + \tilde{\mu} H^2 + \frac{g(\rho_b - \rho_a)}{k} \right)} \quad (2.4)$$

and is depicted in figure 3(a).

So far we have examined the instability in time. However, in our experiment it is advected by the flow and examined in space. For the related stability map, showing the critical velocity as a function of f, an analytical expression cannot be found easily, as a cubic equation must be examined. The numerical solution, however, is shown in figure 3(b). As one can see in figure 3 and (2.4) a magnetic field $H > 0$ stabilizes the system and shifts the neutral curves to higher flow velocities for all wavenumbers and frequencies (cf. blue lines). Its minimum, the velocity of the first unstable waves U_{crit}^0, occurs at the *capillary wavenumber $k_{crit}^0 = \sqrt{g(\rho_a + \rho_b)/\gamma}$* (Cowley & Rosensweig 1967), and is independent of the wavenumber k, as marked in figure 3(a) by the dotted vertical line. In contrast, as illustrated in figure 3(b), the frequency of the minimum depends linearly on the velocity U_{crit}^0 via the convective term $\hat{\omega}$ in (2.3) where $\tilde{\omega} = 0$.

3. Experiments

First we give an overview of the experimental apparatus (§3.1), and then we present the material parameters of the two fluids used in the experiment (§3.2). Thereafter, the method used to measure the flow velocity is described (§3.3). In §3.4, we give details on how the liquid interface is determined from the recorded pictures. Eventually we sketch the magnetic (§3.5) and mechanical (§3.6) devices utilized for the local excitation of waves of preset frequency.

3.1. *Experimental set-up*

The heart of our experimental set-up is sketched in figure 4(a). A straight section of the flow channel, made from Perspex$^©$, harbours the liquid interface in between the ferrofluid on top and a more dense, immiscible and transparent fluid on the bottom. This interface section of the channel has a length of 150 mm (x-direction), a width of 25 mm
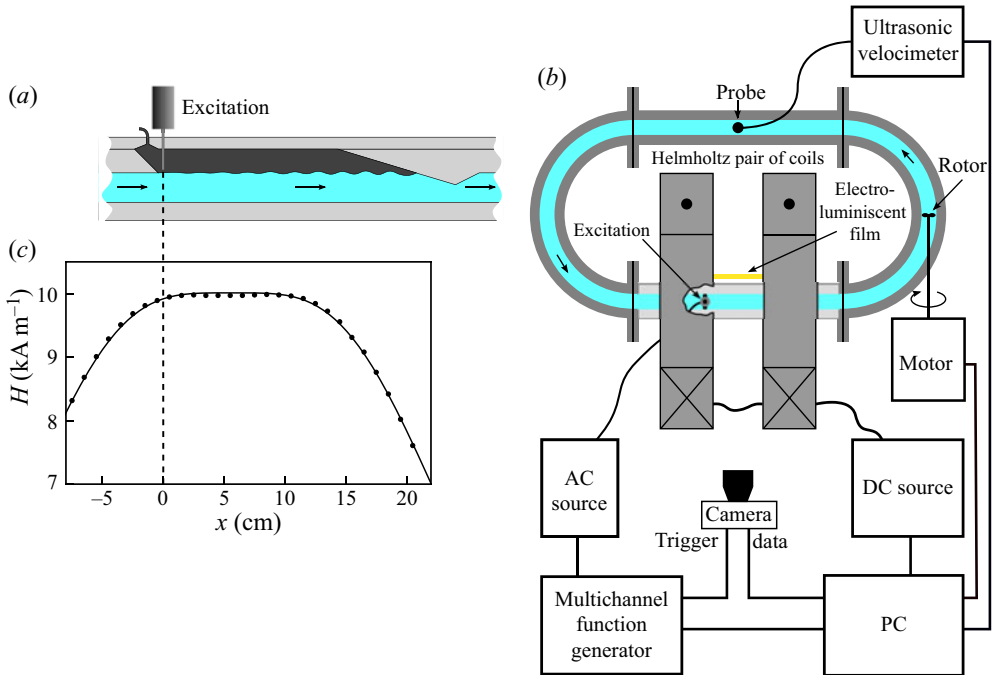
FIGURE 4. Sketch of the flow channel. In its interfacial section the ferrofluid rests on top of a flow of transparent fluid (*a*). The interfacial section is part of a stadium-shaped conduit (*b*) and is placed in the centre of a Helmholtz pair of coils. The magnetic field generated by these coils is matched to the ferrofluidic section of the channel (*c*). The data points denote measurements of the axial magnetic field, while the solid line denotes the calculated values for the applied current of 3.0 A for a Helmholtz pair of coils according to (3.1). The vertical dashed line connecting panels (*a*) and (*c*) marks the position of the exciter, the origin of our coordinate system. A photo of the set-up can be found elsewhere (Völkel, Kögel & Richter 2020).

(*y*-direction) and a height of 45 mm (*z*-direction). Here the flow channel is vertically divided into two sections. The upper one contains 100 ml of ferrofluid, marked black in figure 4(*a*), and has a height of 20 mm. It has a wedged shape of inclination 45° to the horizontal. This sharp edge at the upstream side (left-hand side) serves to foster the shear flow. The ramp at the downstream side (right-hand side), with an inclination of 17°, serves to suppress the standing waves in the channel. Note that the inclined edges also reduce the discontinuity of the magnetization at the up- and downstream sides of the channel. This is similar to the 'radial ramp' introduced by Gollwitzer *et al.* (2007) for measuring the Rosensweig instability in a circular vessel. Moreover, by matching the dimensions of the channel and the Helmholtz pair of coils we have created a 'magnetic beach'. In this way the magnetic field fades out at both ends of the interfacial section. The resulting Kelvin force density $\mu_0(\boldsymbol{M} \cdot \boldsymbol{\nabla})\boldsymbol{H_0}$ (Rosensweig 1985) plus the ramps are sufficient to contain the ferrofluid within the interfacial section of the channel. There are two openings at the top of the channel. The first one, at the upstream side, is used for filling the upper section with ferrofluid, whereas the second one allows the insertion of a magnetic (§ 3.5) or mechanical (§ 3.6) exciter, or a plug. The lower part of the flow channel has a height of 25 mm and a width of 25 mm, and it guides a laminar flow of transparent fluid.

The interface is illuminated from the back by means of an electroluminescent sheet (Zigan displays). To prevent the ferrofluid from wetting the side walls of the channel we attach strongly repellent Teflon© tape (3M™ PTFE Extruded Film Tape 5490) to them. Because the thickness of the tape is 0.09 mm it will hardly accelerate the flow within the channel.

As shown in figure 4(*b*), the interface section of the flow channel, described above, is part of a larger stadium-shaped duct, which is made up of two semi-circles ($d_{inner} = 290$ mm, $d_{outer} = 340$ mm) and two straight sections (length $= 340$ mm), and which harbors 1200 ml of transparent fluid. The latter is put in motion by a propeller with a diameter of 20 mm (cf. right-hand side of figure 4*b*). The flow is relaminarized by a honeycomb structure embedded in the straight section following the propeller. The propeller is driven by an electric motor (Mattke MDR 230/2-4). The latter is controlled via an RS.232 interface by a computer. To minimize electromagnetic disturbances the propeller and the motor are connected via a 340 mm long shaft. Note that a similar channel has worked well for Barchan dunes (Groh, Rehberg & Kruelle 2009). The experimental channel is positioned in the centre of a Helmholtz pair of coils, which allows us to apply a magnetic field oriented parallel to the flow direction of the lower fluid and so parallel to the interface. The coils have a usable clearance of 240 mm (diameter) and 88 mm (distance). Their effective radius is $R = 90$ mm. We measure the magnetic induction B in the empty coils by means of a Hall probe (Lakeshore, MMT-6J02-VH). The applied magnetic field $H = B/\mu_0$ obtained in this way is plotted in figure 4(*c*) by black points. The solid line displays a fit by the equation (Bergmann & Schaefer 2006)

$$H(x) = \frac{NI}{2R} \left\{ \left[\left(\frac{x - x_0}{R} - \frac{1}{2} \right)^2 + 1 \right]^{-3/2} + \left[\left(\frac{x - x_0}{R} + \frac{1}{2} \right)^2 + 1 \right]^{-3/2} \right\}, \quad (3.1)$$

where $x_0 = 5.7$ cm denotes the centre of the Helmholtz pair of coils, $N = 640$ is the number of windings and I is the current. From the measurements we conclude that H does not deviate more than 0.5 % along the visible part of the channel (Kögel 2017). The coils are connected to a direct current source (LAB/SL 230/AI/LT from Eurotest Co.) which is controlled via GPIB interface by the computer.

Pictures of the liquid interface are recorded by a charge-coupled-device (CCD) camera (Lucam Lt225M, Lumenera Co.) which is triggered by a multichannel function generator (TGA1244, TTi Co.) with a frequency of 100 Hz.

3.2. *Properties of the fluids*

For the upper fluid we select the ferrofluid Electro Magnetic Grade (EMG) 909 from Ferrotec Co. Its material parameters are listed in table 1. The magnetization curve $M(H)$ of the ferrofluid has been recorded by means of a vibrating sample magnetometer (VSM), namely Lakeshore 7404 from Cryotech, utilizing a spherical sample holder (Friedrich *et al.* 2012). The $M(H)$ curve and its granulometric characterization by means of a superposition of Langevin functions has been presented by Rehberg, Richter & Hartung (2019), yielding the listed initial susceptibility χ_0. The diamagnetic fluid below is the perfluoroether Galden SV90 from Solvay Solexis, as utilized before (Sterr *et al.* 2008; Poehlmann, Richter & Rehberg 2013). Its susceptibility has been measured by the VSM as well, and is included in table 1 for the sake of completeness. Because of its tiny value it can be neglected. The interfacial tension between the two fluids has been measured by means of a drop volume tensiometer (Lauda TVT2). The densities of both fluids have been determined by

Property	EMG 909	Galden SV 90
density ρ (kg m^{-3})	982	1734
viscosity η (mPa s)	4.2	1.2 ± 0.1
initial volume susceptibility χ_0	0.688	-8.14×10^{-6}
interface tension γ (mN m^{-1})		4.39

TABLE 1. Properties of the fluids EMG 909 (Lot No. H030308A) from Ferrotec Co. and Galden SV90 from Solvay (2017) Solexis.

an electronic density meter (DMA 4100, Anton Paar Co.). The viscosities of both fluids were measured with the rheometer MCR 500 (Anton Paar Co.) utilizing the double gap geometry (type DG 26,7).

3.3. *Velocity measurement*

We measure the velocity profile of the moving fluid with an ultrasonic Doppler velocimeter (DOP 3000 from Signal Processing). We use polyamide particles (Griltex 2A P1) for scattering particles with diameters from 50 to 80 µm and a density of 1005 kg m^{-3}. As the density of the particles is less than the density of the transparent fluid, we measured the speed at which the particles ascend in the fluid. This speed is (3 ± 2) mm s^{-1} and therefore much less than the flow velocity during the experiments, which is typically above 100 mm s^{-1}. Hence we can assume the particles essentially follow the streamlines of the moving fluid. A velocity profile, averaged over six measurements, is shown in figure 5. The large error bars for $y \gtrsim 18$ mm are caused by a non-perfect coupling of the ultrasonic probe to the lid of the channel. Likewise, the measurements are distorted by scattering on different interfaces and the surface of the ultrasonic gel used. As we expect a symmetric velocity profile, the measurements at $y < 18$ mm are sufficient for determining the whole profile. The maximal flow velocity U in the channel was found (Kögel 2017) to depend on the rotation frequency ν of the motor according to

$$U(\nu) = (9.5 \times 10^{-5} \, \nu \, \text{r.p.m.}^{-1} - 4.5 \times 10^{-2}) \, \text{m s}^{-1}.$$

3.4. *Detection of the interface*

In figure 6(*a*) we present a typical photo of the liquid interface between the ferrofluid (above) and the transparent fluid (below). In panel (*b*) we plot the brightness along the vertical line, marked green in (*a*). Each line can be fitted by the error function marked by the red solid line in (*b*). The point of symmetry of the former defines the position of the interface. Panel (*c*) indicates the detected interface by a yellow solid line.

3.5. *Magnetic excitation*

In order to excite a surface wave with a defined frequency f, either a local electric excitation (Leiderer, Ebner & Shinkin 1982), a local blowing (Mahr, Groisman & Rehberg 1996), or a local magnetic excitation (Browaeys *et al.* 1999) has been used for measuring the dispersion relation of a quiescent liquid layer. In our case the challenge was to apply a magnetic induction $B_\perp$, oriented
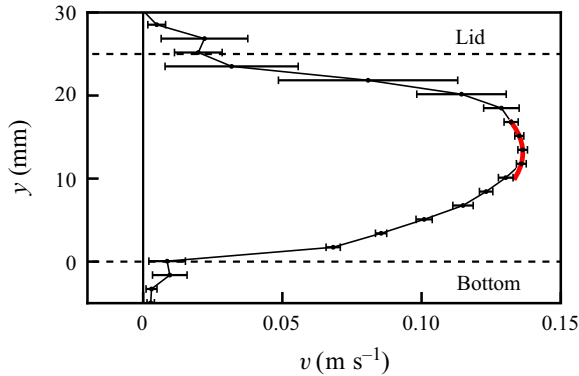
FIGURE 5. Averaged velocity profile $v(y)$ after six measurements at a motor speed of 2000 rpm. The dashed lines indicate the lid ($y = 25$ mm) and the bottom ($y = 0$ mm) of the channel. The red solid line shows a parabolic fit, as a convenient approximation.
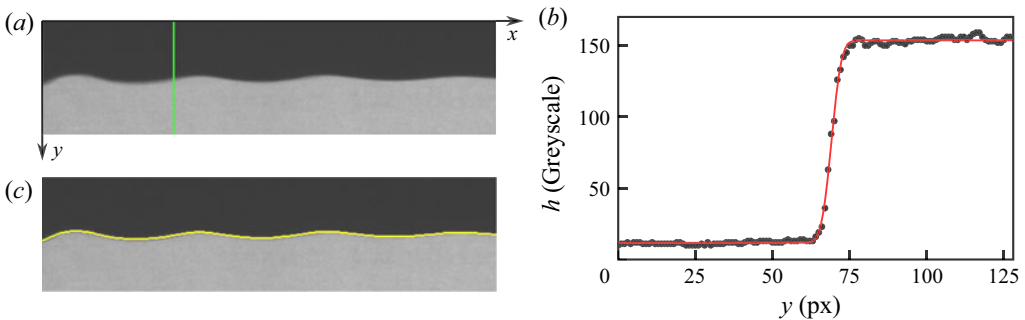

FIGURE 6. Typical photo of the interface (a) and greyscale along one vertical line (b), which is marked green in panel (a). The red solid line denotes a fit by the function $h(y) = A \operatorname{erf}(B(y - y_0)) + h_0$, where erf denotes the error function. The detected typical interface is marked in yellow in panel (c). For display purposes the detected interface was rounded to full pixels.

normal to the interface, at and only at a position x_0 of the interface; i.e. $B_\perp(x) \approx B_\perp^0 \cdot \delta(x - x_0)$. At the same time the induction $B_\perp$ should not vary across the channel; i.e. $B_\perp(y) = $ const. For that purpose an iron sheet (thickness of 2 mm, length of the stem 55 mm, height of the blade 12 mm) was wrapped by a wire ($\varnothing$ 1.0 mm, 70 windings), as shown in figure 7(a). The iron sheet has a grater-like shape, with a triangular cutting edge at its lower end (b). In this way it guides the magnetic flux towards a position 2 mm above the interface. The corners of the blade next to the channel walls are slightly rounded in order to suppress fringe fields there (b). As shown in figure 8(a), the magnetic induction, measured by means of a Hall probe immediately beneath the blade, is still higher at the corners, but does not vary more than 25 % across the width of the channel. Likewise, figure 8(b) presents both components of the induction, measured in the centre of the channel for increasing distance from the exciter. The solid lines indicate fits by an exponential decay, and thus illustrate that the type of excitation is sufficiently local. The magnetic driving is based on the Kelvin force density $f_K = M_{FF}(H) \cdot \partial B / \partial z$ which is acting upon the ferrofluid with magnetization $M_{FF}(H)$. We vary f_K by a periodic modulation of $\partial B / \partial z$ by modulating the magnetization $M_{st}(t)$ of the
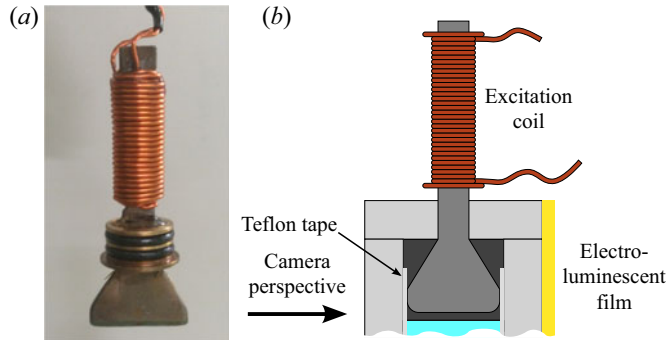
FIGURE 7. Magnetic driving of the interface by means of a local coil with soft iron core (*a*), mounted 2 mm above the interface (*b*).
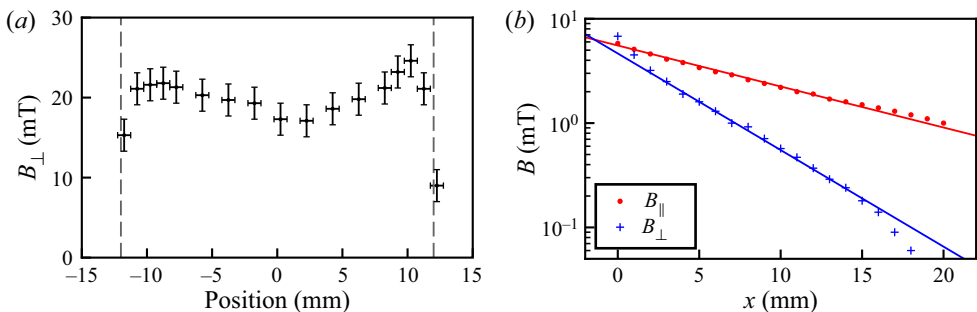

FIGURE 8. Spatial variation of the magnetic induction: (*a*) Vertical component measured directly beneath the blade of the magnetic exciter, where the dashed vertical lines indicate the walls of the channel. (*b*) Horizontal and vertical component of the exciter measured in a distance x down the stream. Here the solid lines mark fits by an exponential decay: $B_\parallel(x) \approx 5.5\ \mathrm{mT} \cdot \exp(-x/11.0\ \mathrm{mm})$, $B_\perp(x) \approx 4.6\ \mathrm{mT} \cdot \exp(-x/4.7\ \mathrm{mm})$. For the measurements a Hall probe (type MNA-1904-VH, from Lakeshore Co.) connected to a Gaussmeter (type 450, from Lakeshore Co.) was used.

steel sheet. This is achieved by driving the coils by a current source (LAB/SL 30 from Eurotest Co.), connecting its voltage contol input to the voltage output of a function generator (TGA1244 from TTi Co.) connected to the computer. For all experiments we selected $U_{DC} = 2.5$ V and $U_{AC} = 5.0$ V, where $U = U_{DC} + U_{AC} \sin(2\pi f t)$ gives the overall applied control voltage.

Figure 9(*a*) displays the discrete Fourier transform (DFT) of the temporal evolution of the interface at distances of $x = 20$ mm (blue), 30 mm (red) and 40 mm (green) downstream of the magnetic exciter. The dominating peaks at 8 Hz prove the efficiency of the driving. The inset provides a zoom of the peaks, which decay with increasing distance x. Likewise, the time-averaged autocorrelation function in figure 9(*b*) shows a decay as well. From its first relative maximum, marked by a red dot, the wavelength λ can be determined.

From the results above as well as from our experience, it follows that the magnetic exciter allows a reliable and smooth driving of the interface. However, an unwanted side effect is the fact that the soft iron core will be magnetized not only by the driving current, but also by the horizontal induction impressed by the static field applied by the Helmholtz
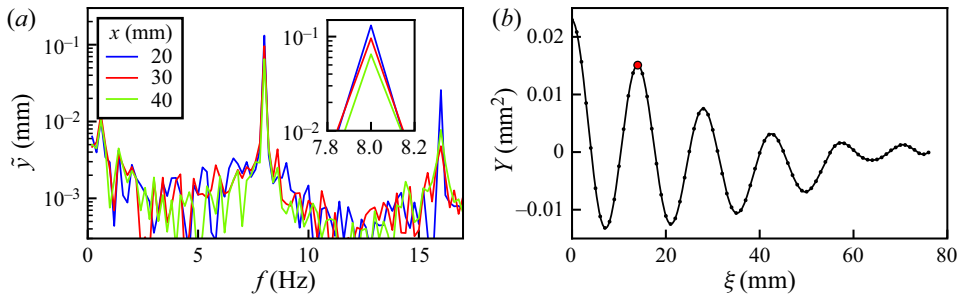
FIGURE 9. Dynamics of the interface for a driving frequency of $f_0 = 8$ Hz, a flow velocity $U = 0.126$ m s^{-1} and a magnetic field $H = 8.0$ kA m^{-1}: (*a*) Digital Fourier transform $\tilde{y}$ of the wave amplitude for three sample x-positions. The inset gives a zoom around the peaks at 8 Hz. (*b*) Averaged autocorrelation function Y vs space. The estimated data are marked by dots, the solid line indicates a fit by a cubic spline, and the red dot denotes the first local maximum.
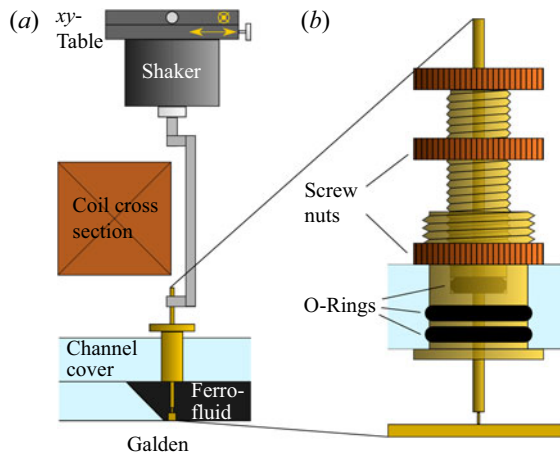

FIGURE 10. Set-up of the mechanical wave exciter, with a horizontal bar at the interface, attached to a vertical shaft (*a*), and detail of the lead-through with O-ring sealing (*b*). Panel (*b*) is rotated against panel (*a*) by 90°.

pair of coils. We therefore investigated as a reference method a mechanical excitation, which is presented next.

3.6. *Mechanical excitation*

The mechanical exciter is sketched in figure 10(*a*). The interface is perturbed by a horizontal bar (see blow-up in panel *b*) connected via a vertical shaft to an electro-mechanical vibration exciter (Brüel & Kjær, type 4810, with amplifier type 2706). The bar has a length of 24.7 ± 0.1 mm, thus filling almost the whole width of the channel. A lead-through with adjustable O-ring allows a leak-tight reciprocating motion of the shaft. Bar, shaft and lead-through are made from brass, a material with negligible susceptibility. The shaft is attached to a U-shaped module (made from aluminium), which transfers the motion, bypassing one of the coils.
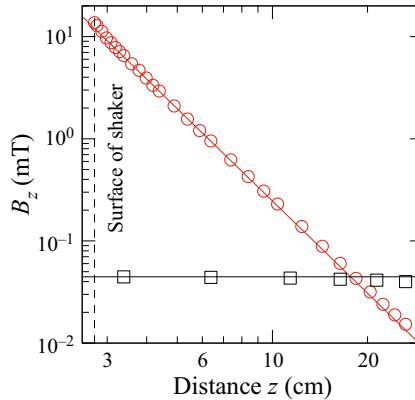
FIGURE 11. Decay of the constant stray field vs distance measured by means of a Hall probe (filled red circles). The red solid line represents a fit by $B_z(z) = \mu_0 \, m/(2\pi z^3)$, with $m = (1.23 \pm 0.03)$ Am^2. The open black squares give the data of the magnetic background.

We have measured the magnetic stray field of the exciter by means of a Hall probe (type MNT-4E02-VG, from Lakeshore Co.), as marked in figure 11 by red circles. The solid line displays the characteristic decay of $B(z)$ on the axis of a dipole. Already at a distance of 200 mm the stray field is below the bias (marked by squares) determined by the earth's magnetic field. Thus we have positioned the shaker 220 mm above the flow channel. For a reliable, stick-free driving it is important to fine-tune the position of the shaker in the plane by a micrometre stage for the x- and by one for the y-direction.

The mechanical driving might be expected to outperform the magnetic one, because it does not perturb the applied magnetic field. However, it turned out to depend sensitively on the position of the meniscus at the driving bar, as illustrated in figure 12. In panel (*a*) the interface is pinned by the lower edge of the bar, as indicated by the red arrow, whereas in panel (*b*) the interface is not pinned. In panel (*c*) we plot the driving amplitude vs the distance from the exciter, measured for two sample flow velocities. The driving amplitude shows only a weak dependence on the flow velocity for the pinned menisci (solid lines) but a strong dependence for the unpinned menisci (dashed lines). Therefore, prior to measurements, the meniscus was carefully pinned at the lower edge. More details are given by Fischer (2017). As in § 3.5 we show in figure 13 the DFT of the temporal evolution of the interface for three chosen driving frequencies. The amplitude at the excitation frequency (indicated by arrows) is clearly dominating the spectra.

4. Experimental results

In the following we give experimental evidence of a calming of the waves by a magnetic field (§ 4.1) and present exemplary measurements of the growth rates of the interface undulations (§ 4.2), the stability diagrams derived therefrom (§ 4.3), and eventually the measured dispersion relation (§ 4.4).

4.1. *Experimental evidence*

The application of a tangential magnetic field has immediate impact on the amplitude of the interfacial waves. Figure 14(*a*) shows a snapshot of spontaneous waves. When an induction of $B = 10$ mT is applied, the amplitudes are considerably damped, as presented
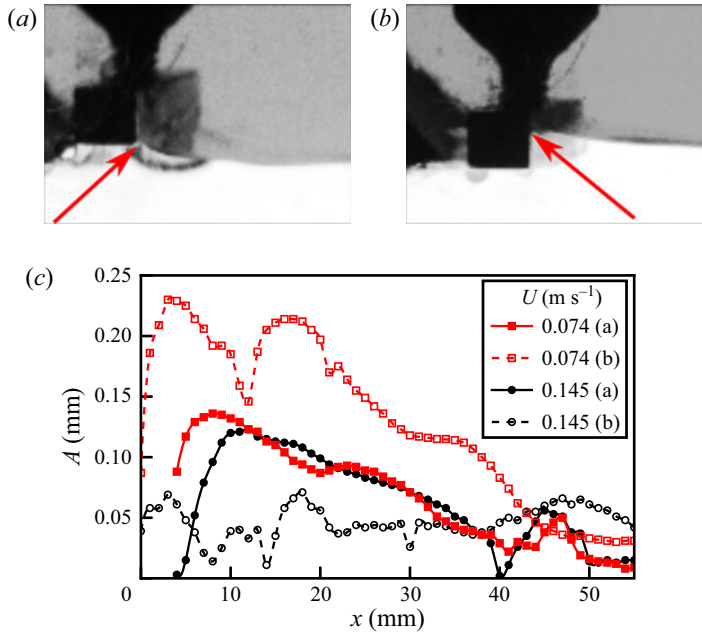
FIGURE 12. Effect of the pinning of the meniscus on the driving: pinned (*a*) and loose (*b*) menisci, as indicated by red arrows, at the horizontal bar of the exciter, and related amplitudes *A* vs distance *x* from the exciter measured for two different flow velocities *U*, as denoted by the inset (*c*).
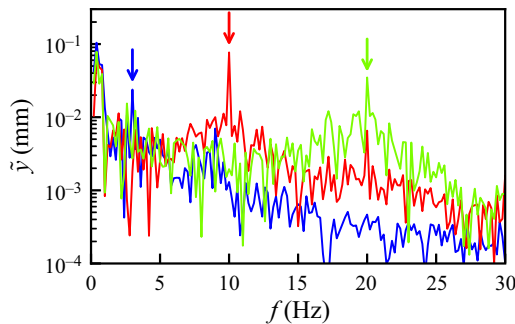

FIGURE 13. Frequency spectrum of the interface at a distance of 10 mm downstream of the mechanical exciter, for an excitation with $f_0 = 3$ Hz (blue), 10 Hz (red) and 20 Hz (green). The excitation frequency is annotated by arrows. The flow velocity was 0.145 m s^{-1}.

in figure 14(*b*). From the snapshot in figure 14(*a*) it becomes clear that the spontaneously generated waves show a broad spectrum of wavelengths. For a sensible comparison with the model of § 2 it is advantageous to excite waves of a preset frequency *f* (and wavelength) by magnetic or mechanical means, as shown in figures 14(*c*) and 14(*e*), respectively. Likewise figures 14(*d*) and 14(*f*) demonstrate the calming effect of a horizontal magnetic field at the same parameters. Next we exploit this arrangement for measuring the growth rates of the interfacial waves.

FIGURE 14. Experimental evidence for a calming of the interfacial waves at $U = 0.192$ m s^{-1}. Spontaneously emerging waves without an externally applied magnetic induction (*a*), and for $B = 10$ mT (*b*). Magnetically generated waves without (*c*) and with (*d*) applied induction $B = 10$ mT. Mechanically generated waves without (*e*) and with (*f*) applied induction $B = 10$ mT. A movie demonstrating this effect when switching on B can be accessed at https://doi.org/10.1017/jfm.2020.642. The frames have a size of 117 mm × 10 mm.

4.2. *Growth rates*

First we utilize the magnetic exciter (see § 3.5), which defines the position $x = 0$ mm in our frame of reference, and apply a driving with frequency $f \in [6$ Hz, 20 Hz]. For each position x along the interface we determine the amplitude $A(x)$ of surface undulations by means of a DFT. As an example we illustrate the outcome of this procedure in figure 15(*a*) for $f = 11$ Hz and four sample flow velocities U. For the subcritical flow velocities ($\cdot$, $\circ$) the amplitude decays, whereas for supercritical values ($\square$, $\diamond$) it grows downstream of the exciter. In the interval [0 mm, 20 mm] the amplitude $A(x)$ appears to follow an exponential law

$$A = A_0 \exp(\alpha x), \tag{4.1}$$

where α denotes the growth or decay rate along x. The corresponding fits are marked in figure 15(*a*) by solid lines. Further from the exciter the growth of $A(x)$ does not follow the linear stability analysis (4.1), possibly due to the viscosity and the friction at the side walls, which is not taken into account in the simple ansatz.

The growth rates α determined from these fits depend sensitively on U, but also on the horizontally applied magnetic field H, as shown in figure 15(*b*). For a fixed field H the growth rate α increases with U, becoming unstable at $\alpha(U_{crit}) = 0$. Increasing the field H
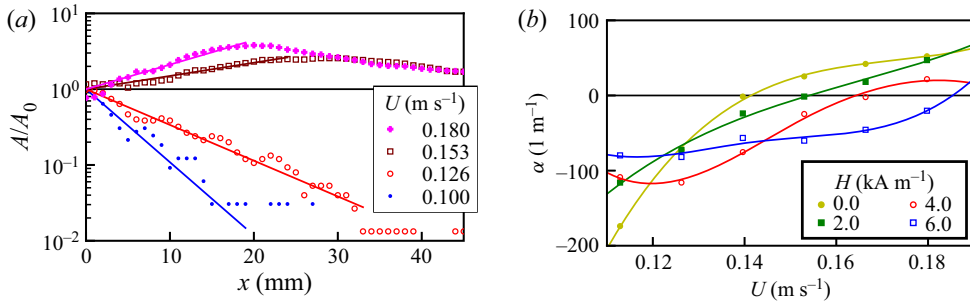
FIGURE 15. Growth of surface waves: (*a*) amplitude vs the distance from the exciter along the direction of the flow at a driving frequency of $f = 11$ Hz without horizontal magnetic induction, i.e. $B_x = 0$ mT. The inset indicates the symbols marking four different flow velocities. The straight lines denote an exponential fit by (4.1). (*b*) The data points indicate the measured growth rates vs the flow velocity for different values of the horizontally applied magnetic induction. To guide the eyes the data points are interpolated by cubic splines (solid lines).

shifts the $\alpha(U)$ curves to the right, thereby shifting U_{crit} to higher velocities. In this way the interface remains stable up to a higher velocity.

In order to check the reliability of the magnetic driving we have performed similar experiments utilizing the mechanical exciter described in § 3.6. Figure 16 compares the two methods of excitation for two representative values of the applied magnetic field. Data points obtained with the mechanical bar are denoted by squares (□), and those with the magnetized wedge by a triangle (▽). To guide the eyes the data are interpolated by splines. For both types of excitation the critical growth rate U_{crit} is shifted with H to higher values by about the same amount (dashed, $\Delta U_{crit.mech} = 0.017$ m s^{-1}; solid, $U_{crit.mag} = 0.018$ m s^{-1}). Indeed, the differences for ΔU_{crit} are well situated in the range of the error bars. Because the magnetic driving is more robust – it does not sensitively depend on the proper pinning of the meniscus – we present in the remainder of the article solely the data obtained by magnetic excitation.

4.3. *Stability diagrams*

4.3.1. *Periodically excited waves*

We have determined U_{crit} for different driving frequencies and applied magnetic fields. Three exemplary sets of data are shown in figure 17(*a*) together with solid lines calculated via (2.4) for the material parameters of table 1. The data points for zero magnetic field (·) are well described by the basic inviscid model. This is especially true for the interval [10 Hz, 20 Hz]. At lower f the increase of the experimental values is delayed when compared with the inviscid model. At a magnetic field of $H = 4.0$ kA m^{-1} the experiment (○) and the inviscid model are in closer agreement in the same interval, i.e. [5 Hz, 10 Hz]. Here, however, the experimental data exceed the model predictions in between 14 and 20 Hz. For $H = 8.0$ kA m^{-1} (□) the agreement seems to become better again. However, here the error bars are quite large, because U_{crit} needs to be estimated by extrapolation. Comparing the three curves in figure 17(*a*) it is obvious that with increasing magnetic field the stability curves are shifted to higher values. This reflects the calming of the waves. Indeed, as shown in figure 17(*b*) for an exemplary driving frequency of $f = 10$ Hz, the measured critical velocity follows very well the predicted curve (blue solid line). At lower H (red line) the agreement is less convincing.
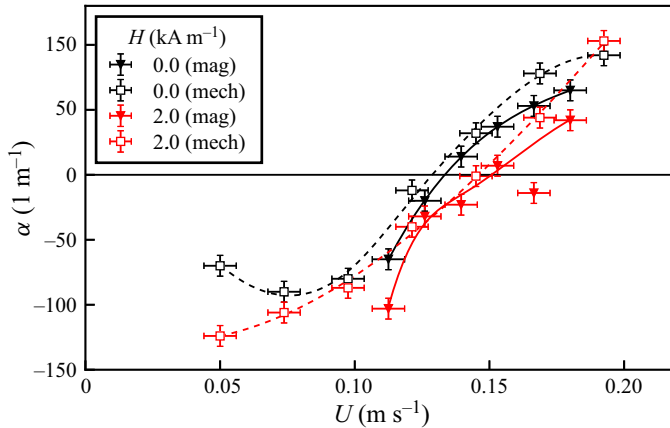
FIGURE 16. Comparison of the growth rates for waves generated with a modulated magnetized iron wedge (∇) and mechanical driving with a bar with square cross-section ($\square$) for different horizontally applied fields H and various flow velocities at $f = 10$ Hz. The amplitude of the mechanical exciter was 0.14 mm. To guide the eyes the data are interpolated by splines (omitting the outlier at $U = 0.166$ m s^{-1} for $H = 2.0$ kA m^{-1}).
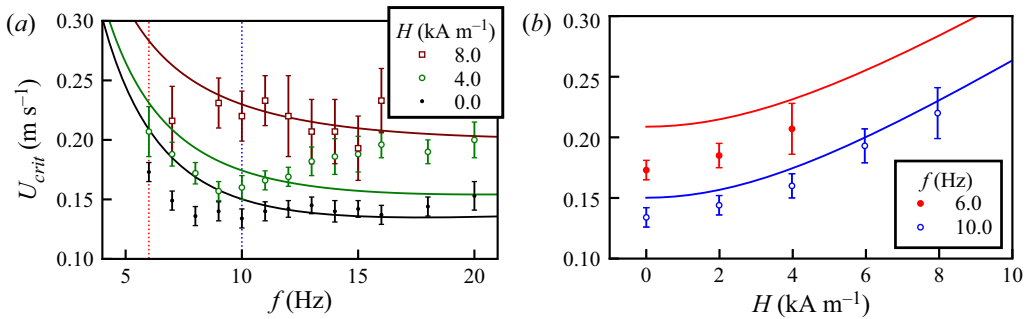

FIGURE 17. (*a*) Critical flow velocity vs driving frequency for three exemplary magnetic fields. The dashed vertical lines indicate the frequency scans for $f = 6.0$ and 10.0 Hz displayed in panel (*b*). The solid lines represent the inviscid model (2.4).

All in all the basic inviscid model, which has no free parameter, captures the measured stability diagrams rather well. Deviations may stem from the difficulty of defining an effective jump of the flow velocity in the experiment. For an in-depth discussion the reader is referred to § 5.

4.3.2. *Spontaneously emerging surface waves*

So far we have investigated the stability of surface waves generated by a periodic driving. Two exemplary curves without (with) a magnetic field are marked in figure 18 by black data points. The solid lines indicate the predictions by the basic inviscid model. With respect to these stability diagrams it is interesting to see that the spontaneously generated surface waves, denoted by red diamonds, are situated slightly above, but apparently fit rather well to the theoretical stability curve (black solid line). However, we point out that the agreement along the x-axis is less convincing because the spontaneously generated waves are not located at the minimum of the stability curve. The minimum is situated in
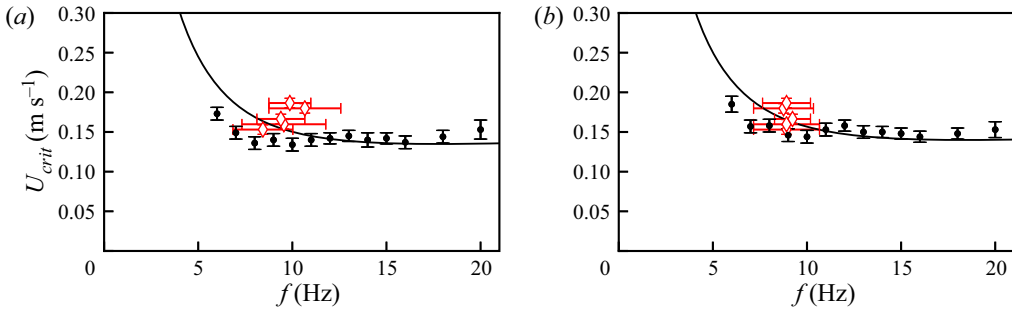
FIGURE 18. Comparison of the measured critical velocity for periodically excited waves (black points) and spontaneously emerging waves (red diamonds), without magnetic field (*a*), and with $H = 2.0\,\text{kA m}^{-1}$ (*b*). The solid line indicates the prediction by the basic inviscid model.
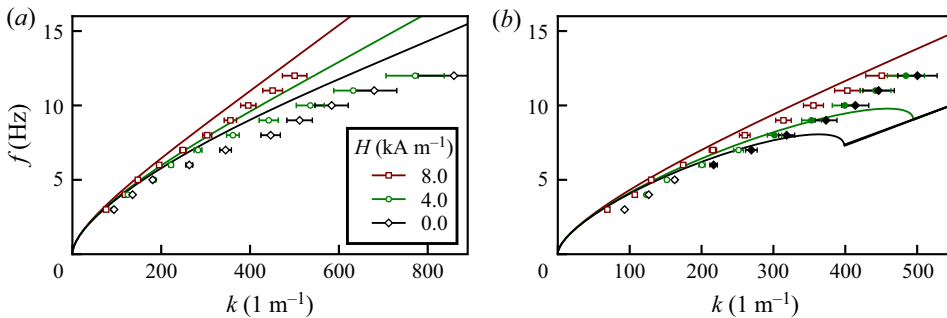

FIGURE 19. Dispersion relation for $U = 0.126\,\text{m s}^{-1}$ (*a*) and $U = 0.180\,\text{m s}^{-1}$ (*b*) and three different magnetic fields. The open (filled) data points mark experimental results for stable (unstable) surface waves, respectively. The lines indicate the outcome of the inviscid model (2.2).

figure 18(*a*) at 16.5 Hz and in figure 18(*b*) at 17.2 Hz. These large differences in *f* may be attributed to the broad footing of the stability curves.

These spontaneous surface waves emerge because the flow generated by the propeller is not completely laminar. Despite a relaminarization duct realized by a honeycomb structure in the straight section following the propeller, fluctuations of the interface may emerge. This is in agreement with the Reynolds number ranging from $Re = 4600$ to $Re = 6300$ for the measurements in figure 18.

4.4. *Dispersion relation*

In § 2 we have presented in (2.2) the dispersion relation for interfacial waves at the KHI. Our experimental arrangement can also be used to measure this relation. Experimental results are plotted in figure 19 for three representative magnetic fields. We have measured the dispersion relation for nine different velocities $U \in [0.1, 0.207]\,\text{m s}^{-1}$. For brevity and clarity we selected one *U* with fully stable surface waves (*a*) and one *U* exhibiting the transition to unstable surface waves (*b*). Figure 19(*a*) shows the measured data for $U = 0.126\,\text{m s}^{-1}$ and compares it with the predictions of the simple inviscid model (marked by solid lines). The $f(k)$ curves, numerically obtained from (2.2), increase monotonically, and with increasing *H* their inclination rises. This is true for the measured data as well as

for the numerical results. However, the latter overestimate the measured data considerably. For example, at $k = 400$ m^{-1} and $H = 8.0$ kA m^{-1}, experiment and model differ by 13 %.

The dispersion relation is more complex at a flow velocity of $U = 0.180$ m s^{-1}, as displayed in figure 19(*b*). Whereas for $H = 8$ kA m^{-1} all measured data (brown squares) indicate a stable interface, as do the numerics (solid line), one finds for $H = 4$ kA m^{-1} (marked green) above $k \approx 300$ m^{-1} the emergence of a convective unstable state, indicated by filled symbols. The numerical solution of (2.2) also predicts a band of unstable wavenumbers, albeit starting at higher k, namely at the kink at $k \approx 500$ m^{-1}. Likewise, for $H = 0$ kA m^{-1}, convective unstable waves are measured for $k \gtrsim 300$ m^{-1}, whereas the kink predicted by the model is situated at $k \approx 400$ m^{-1}. Again all qualitative features of the dispersion relation are met by the basic inviscid model, whereas one finds a quantitative discrepancy in the onset of the unstable band.

5. Summary, discussion and outlook

In a tabletop flow channel we have measured the linear stability of interface waves in between a flow of diamagnetic liquid (on the bottom) and a resting layer of ferrofluid (on the top) – a realization of the Kelvin–Helmholtz instability. We have provided the first experimental evidence that a magnetic field oriented tangential to the liquid surface is capable of calming spontaneously emerging waves. To enable a quantitative comparison with the basic inviscid model reported by Rosensweig (1985), we have periodically perturbed the interface by magnetic or mechanical means. From the zero point of the measured growth rates we have determined the critical flow velocity $U_{crit}(f, H)$. For $H = 0$ and $H = 10$ kA m^{-1} the basic inviscid model (2.2) captures $U_{crit}(f, H)$ well, when taking into account that there is no free parameter. It is notable that the characteristic increase in the critical velocity, which is similar to a hyperbolic curve, is also seen in the experiment. Moreover we have presented experimental data of the dispersion relation $f(k, H)$ at two sample flow velocities. Again the basic inviscid model (2.2) predicts an increase of the wavenumber with the driving frequency, in agreement with the experimental findings. Bands of unstable wavenumbers are found both in the model and in the experiments, albeit over different ranges of k.

In summary, the experiment provides evidence for a calming of interface waves under impact of a tangential magnetic field. Both the critical flow velocity $U_{crit}(f, H)$ and the dispersion relation $f(k, H)$ display most of the qualitative features predicted by the basic inviscid model.

Quantitative discrepancies may stem from three simplifications:

(i) The measured velocity, as shown in figure 5, is apparently not constant across the channel, a simplifying assumption used in § 2. In contrast, for deriving the governing equations, Rosensweig (1985) assumes a jump in the velocity profile at the interface which is only possible for an inviscid moving fluid. In our experiments, however, the moving fluid has a finite viscosity which leads to a continuous velocity profile that is zero at the channel walls. To compare the inviscid model with our measurements, a characteristic velocity had to be chosen. For simplicity we selected the maximum velocity in the centre of the channel. When instead the average velocity was selected (not shown here), the agreement was less convincing.

(ii) Moreover, quantitative deviations may stem from the fact that due to the finite viscosities of both fluids the quiescent upper fluid is advected by the lower one, and consequently the velocity gradient at the interface is further diminished. To estimate

FIGURE 20. A section (110 mm × 19.2 mm) of the upper part of the flow channel. Instead of ferrofluid it is filled with a suspension of tracer particles in water. The impressed flow velocity was $U = (0.207 \pm 0.006)$ m s^{-1}, the exposure time $t_{exp} = 500$ ms. The black dashes mark streaks, indicating the propagation of the tracer particles during t_{exp}.

that effect, the ferrofluid was replaced by a suspension of tracer particles (Iriodin 100 Perlglanz) in water. A vertical laser sheet was oriented parallel to the inner vertical wall of the channel in a distance of 5 mm. Figure 20 presents the recorded image, in which the greyscale has been inverted. The black layer on top indicates the lid of the upper channel, the ramp can be seen on the left, and the liquid interface to the transparent perfluoroether can be seen at the bottom. The black streaks demonstrate the amount of advection. The flow velocity estimated from these streaks is 6 mm s^{-1} when averaged over all parts of the upper section, and 17 mm s^{-1} at its maximum. The flow velocity in the lower channel is therefore 12 (respectively, 33) times higher than the advected flow.

(iii) The detection of the liquid interface had to be recorded at the side walls of the vessel, where the flow is attenuated. The use of a light sheet to record the evolution of the interface in the centre of the channel was prevented by the poor reflectivity of ferrofluid. A more advanced method, namely the attenuation of X-rays, would in principle allow the interface to be measured far away from the container edges (Richter & Bläsing 2001). This method is well established for static interfaces of the Rosensweig instability (Richter & Lange 2009), and has recently been utilized by Poehlmann *et al.* (2013) for measuring the related Rayleigh–Taylor instability in a rotating tangential magnetic field. However, in its present implementation this method is too slow to catch the fast evolution of the interface at the KHI. For that purpose an X-ray source with much higher luminosity and a faster detector are essential.

Notwithstanding the difficulties in comparing a basic model with measurements, the tried and tested macroscopic flow channel has its benefits: it confines a suitable volume of the expensive ferrofluid in its interfacial section by means of two inclined ramps and a carefully matched magnetic field, which is also ramped. In this way it permits for the first time the continuous measurement of the KHI for a superparamagnetic/diamagnetic liquid interface. This would not be possible in a tilting-tube configuration as used by Thorpe (1968, 1969), which generates an accelerated flow.

Declaration of interests

The author report no conflict of interest.

Supplementary movies

Supplementary movies are available at https://doi.org/10.1017/jfm.2020.642.

REFERENCES

BARKOV, Y. D. & BASHTOVOI, V. G. 1977 Experimental investigation of instability in a plane layer of magnetizable fluid. *Magnetohydrodynamics* **13** (4), 497–499.

BERCEGOL, H., CHARPENTIER, E., COURTY, J. M. & WESFREID, J. E. 1987 Anisotropy effects in ferrofluid instabilities. *Phys. Lett.* A **121** (6), 311–316.

BERGMANN, L. & SCHAEFER, C. (Ed.) 2006 *Lehrbuch der Experimentalphysik/2. Elektromagnetismus*, 9th edn. de Gruyter.

BROWAEYS, J., BACRI, J.-C., FLAMENT, C., NEVEU, S. & PERZYNSKI, R. 1999 Surface waves in ferrofluids under vertical magnetic field. *Eur. Phys. J.* B **9**, 335–341.

COWLEY, M. D. & ROSENSWEIG, R. E. 1967 The interfacial stability of a ferromagnetic fluid. *J. Fluid Mech.* **30**, 671.

D'ANGELO, N. 1965 Kelvin–Helmholtz instability in a fully ionized plasma in a magnetic field. *Phys. Fluids* **8** (9), 1748–1750.

D'ANGELO, N. & GOELER, S. V. 1966 Investigation of the Kelvin–Helmholtz instability in a cesium plasma. *Phys. Fluids* **9** (2), 309–313.

ELHEFNAWY, A. R. F. 1995 The effect of magnetic fields on the nonlinear instability of two superposed magnetic streaming fluids, each of a finite depth. *Can. J. Phys.* **73** (3-4), 163–173.

ELHEFNAWY, A. R. F. & MOATIMID, G. M. 2001 Nonlinear dynamics and stability of two streaming magnetic fluids. *Chaos, Solitons Fractals* **12** (7), 1207–1216.

FISCHER, A. 2017 Magnetische Wellenstillung. Bachelor thesis, Universität Bayreuth, Bayreuth, Germany.

FOULLON, C., VERWICHTE, E., NAKARIAKOV, V., NYKYRI, K. & FARRUGIA, C. J. 2011 Magnetic Kelvin–Helmholtz instability at the sun. *Astrophys. J. Lett.* **729** (1), L8.

FRIEDRICH, T., LANG, T., REHBERG, I. & RICHTER, R. 2012 Spherical sample holders to improve the susceptibility measurement of superparamagnetic materials. *Rev. Sci. Instrum.* **83** (4), 045106.

FRIEDRICHS, R. 2002 Low symmetry patterns on magnetic fluids. *Phys. Rev.* E **66**, 066215.

FRIEDRICHS, R. & ENGEL, A. 2001 Pattern and wave number selection in magnetic fluids. *Phys. Rev.* E **64**, 021406.

GAILITIS, A. 1977 Formation of the hexagonal pattern on the surface of a ferromagnetic fluid in an applied magnetic field. *J. Fluid Mech.* **82** (3), 401–413.

GOLLWITZER, C., MATTHIS, G., RICHTER, R., REHBERG, I. & TOBISKA, L. 2007 The surface topography of the Rosensweig instability: a quantitative comparison between experiment and numerical simulation. *J. Fluid Mech.* **571**, 455–474.

GROH, C., REHBERG, I. & KRUELLE, C. A. 2009 How attractive is a barchan dune? *New J. Phys.* **11** (2), 023014.

GROH, C., RICHTER, R., REHBERG, I. & BUSSE, F. H. 2007 Reorientation of hexagonal patterns under broken symmetry: hexagon flip. *Phys. Rev.* E **76**, 055301(R).

VON HELMHOLTZ, H. 1868 On discontinuous movements of fluids. *Phil. Mag.* **36**, 337–346.

THE HOLY BIBLE: KJV EMERALD TEXT BIBLE 2006 Cambridge University Press.

KÖGEL, A. 2017 Experimentelle Untersuchung zur magnetisch beeinflussten Kelvin–Helmholtz-Instabilität. Master thesis, Universität Bayreuth, Bayreuth, Germany.

LANDERER, R. (Ed.) 1894 *Beruhigung der Wellen durch Oel*, Schiffahrt, Schiffbau, Häfen edn, vol. 31. Hansa.

LEIDERER, P., EBNER, W. & SHINKIN, V. B. 1982 Macroscopic electronic dimples on the surface of liquid Helium. *Surf. Sci.* **113**, 405–411.

LI, X., ZHANG, J., YANG, S., HOU, Y. & ERDÉLYI, R. 2018 Observing Kelvin–Helmholtz instability in solar blowout jet. *Sci. Rep.* **8** (1), 8136.

MAHR, T., GROISMAN, A. & REHBERG, I. 1996 Non-monotonic dispersion of surface waves in magnetic fluids. *J. Magn. Magn. Mater.* **159**, L45–L50.

MALIK, S. K. & SINGH, M. 1992 Chaos in Kelvin–Helmholtz instability in magnetic fluids. *Phys. Fluids* A **4** (12), 2915–2922.

POEHLMANN, A., RICHTER, R. & REHBERG, I. 2013 Unravelling the Rayleigh–Taylor instability by stabilization. *J. Fluid Mech.* **732**, R3.

REHBERG, I., RICHTER, R. & HARTUNG, S. 2019 Graphical magnetogranulometry of EMG 909. *J. Magn. Magn. Mater.* **505**, 166868.

REIMANN, B., RICHTER, R., KNIELING, H., FRIEDRICHS, R. & REHBERG, I. 2005 Hexagons become the secondary pattern if symmetry is broken. *Phys. Rev.* E **71**, 055202(R).

RICHTER, R. & BLÄSING, J. 2001 Measuring surface deformations in magnetic fluid by radioscopy. *Rev. Sci. Instrum.* **72**, 1729–1733.

RICHTER, R. & LANGE, A. 2009 Surface instabilities of ferrofluids. In *Colloidal Magnetic Fluids: Basics, Development and Applications of Ferrofluids* (ed. S. Odenbach), Lecture Notes in Physics, vol. 763, chap. 3, pp. 157–243. Springer.

ROSENSWEIG, R. E. 1985 *Ferrohydrodynamics*. Cambridge University Press.

SCHEIDT, D. 2012 Analyse der Einflüsse auf den Energieverbrauch bei Containerschiffen und Entwicklung von Indikatoren zur Bewertung der Energieeffizienz. Master's thesis, TU Hamburg-Harburg, Hamburg, Germany.

SCOTT, J. C. 1978 The historical development of theories of wave-calming using oil. *Hist. Technol.* **3**, 163–186.

SOLVAY. 2017 Galden PFPE. Available at: http://www.solvay.com/en/markets-and-products/featured-products/Galden.html.

STERR, V., KRAUSS, R., MOROZOV, K. I., REHBERG, I., ENGEL, A. & RICHTER, R. 2008 Rolling ferrofluid drop on the surface of a liquid. *New J. Phys.* **10** (6), 063029.

SUTYRIN, G. G. & TAKTAROV, N. G. 1975 On the stability of a tangential discontinuity in a magnetizable medium: Prikladnaya Matematika i Mekhanika vol. 39, nr 3, 1975, pp. 547–550. *J. Appl. Math. Mech.* **39** (3), 520–524.

THOMSON, W. 1871 Hydrokinetic solutions and observations. *Phil. Mag.* **42**, 362–377.

THORPE, S. A. 1968 A method of producing a shear flow in a stratified fluid. *J. Fluid Mech.* **32** (4), 693–704.

THORPE, S. A. 1969 Experiments on the instability of stratified shear flows: immiscible fluids. *J. Fluid Mech.* **39** (1), 25–48.

TSIMPLIS, M. N. 1991 The effect of rain in calming the sea. *J. Phys. Oceanogr.* **22**, 404–412.

VÖLKEL, A., KÖGEL, A. & RICHTER, R. 2020 Measuring the Kelvin–Helmholtz instability, stabilized by a tangential magnetic field. *J. Magn. Magn. Mater.* **505**, 166693.

YECKO, P. 2009 Stability of layered channel flow of magnetic fluids. *Phys. Fluids* **21** (3), 034102.

YECKO, P. 2010 Effect of normal and parallel magnetic fields on the stability of interfacial flows of magnetic fluids in channels. *Phys. Fluids* **22** (2), 022103.

ZAKARIA, K. 2003 Nonlinear dynamics of magnetic fluids with a relative motion in the presence of an oblique magnetic field. *Physica* A **327** (3–4), 221–248.

ZELAZO, R. E. & MELCHER, J. R. 1969 Dynamics and stability of ferrofluids: surface interactions. *J. Fluid Mech.* **39**, 1–24.